🔓 **Open Access**

Ultrasonic Sensitivity-Improved Fabry–Perot Interferometer Using Acoustic Focusing and Its Application for Noncontact Imaging

Qiangzhou Rong
Ruixiang Zhou
Yongxin Hao
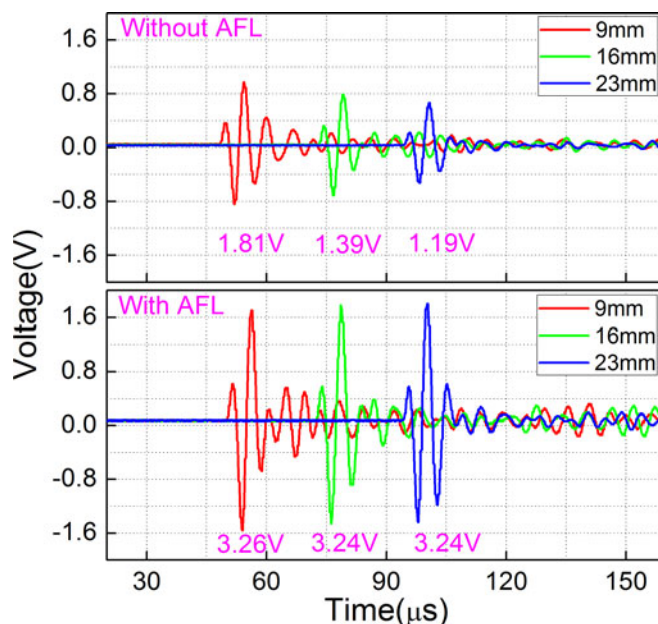Xunli Yin
Zhihua Shao
Tingting Gang
Xueguang Qiao

photonics
SOCIETY

IEEE

Ultrasonic Sensitivity-Improved Fabry–Perot Interferometer Using Acoustic Focusing and Its Application for Noncontact Imaging

Qiangzhou Rong,[1] **Ruixiang Zhou,**[1] **Yongxin Hao,**[1] **Xunli Yin,**[1,2]
Zhihua Shao,[1] **Tingting Gang,**[1] **and Xueguang Qiao**[1]

[1]Department of Physics, Northwest University, Xi'an 710069, China
[2]School of Physics, Xi'an Shiyou University, Xi'an 710065, China

Abstract: An easily multiplexed fiber-optic Fabry–Perot interferometer (FPI)-based ultrasonic wave (UW) sensor has been proposed and used to experimentally demonstrate ultrasound wave imaging of seismic-physical models. The sensor probe comprises an interferometer formed by a free-standing gold foil and a cleaved optic-fiber tip. An acoustic focusing lens enhances the sensor's ultrasound sensitivity and assists with capability to multiplex multiple probes. Theoretical modeling of the focusing effect of the acoustic lenses and the ultrasonic responses of the probes are presented and analyzed. We present an experimental demonstration of time-division multiplexing of three fiber-optic Fabry–Perot sensors operating in air to reconstruct the shapes of physical models. The compact sensor has a symmetrical structure so that it presents a good directionality of ultrasound detection, making it valuable as an effective sensor for ultrasound scanning of physical models in air.

Index Terms: Fabry-Perot interferometer (FPI), ultrasonic imaging, acoustics focusing.

1. Introduction

Ultrasonic wave (UW) detection is one of the most important techniques for nondestructive testing of seismic physical models. Such testing effectively bridges the gap between theory and field-scale experiments, thereby allowing us to study changes of the acoustic response in absence of a rock matrix in a nearly ideal setting [1]–[4]. The UW detection is traditionally realized using current-driven piezoelectric transducers (PZTs) [5]–[7]. However, there are several drawbacks to this kind of transducer: the large structure size limits the spatial resolution of the device; the materials used to fabricate the detectors are sensitive to electromagnetic disturbances; the response frequency bandwidth is narrow owing to the resonant detection mechanism; and the sensitivity is so low that it is usually necessary to use acoustic coupling agents such as water and water soluble polymer colloids. As an alternative to PZTs, fiber-optic UW sensors have attracted great interest because of their

unique properties. These fiber-optic sensors have opened up a multitude of opportunities for single-point ultrasonic sensing in hard-to-reach environment of electromagnetic field with controllable cross-sensitivities and very compact size for embedded measurement with ultra-high sensitivity [8]–[12]. To date, the spectral band-side filtering technique, which is usually used for the UW interrogation, requires that the sensor has a stable linear spectral slope [13], [14]. Among reported fiber UW sensors, fiber Fabry-Perot interferometers (FPIs) have frequently been chosen because of their advantageous characteristics, which include compact size, flexible structure and high stability (low frequency vibration resistance) [15]–[18]. The sensitivity of the FPI is determined by the structure and materials of the interferometer cavity. A diverse range of optical films such as thin silica [19], graphene [20], and parylene-C polymer [21] have been employed for forming the FPIs for UW detection. Typically, these types of fiber FPIs have been used as hydrophones. However, their low reflectivity and multilayer structure result in low signal-to-noise ratio (SNR) as well as the fabrication processes are complex. Besides, these fiber FPI hydrophones need to be immersed in water, which is a transmission medium with relatively low acoustic attenuation (0.0018 dB/cm at 300 kHz). The hydrophones have needed waterproof packaging to ensure the sensitivity and stability of the immersed sensors. Ability to easily and efficiently multiplex sensors is another important characteristic of fiber UW sensors. The sensors mentioned above could work as single probes, but are difficult to multiplex. For fiber FPI-based sensors, the time-of-flight in a fiber delay line is a standard method to distinguish the collected UW signal from the different sensors [22]–[25]. Although an all-fiber system could be achieved, the complex transmission line and large light loss were the problems that limited the multiplexing capability of the sensors. An alternative solution which we will explore is to employ the FPI cavity itself as a time delay line.

In this paper, we propose and demonstrate a multiplexed fiber FPI UW detector using an acoustic focusing lens (AFLs) to effectively focus the acoustic wave onto the sensing surface of the FPI. The FPI cavity comprises a flexible, partially reflective ultra-thin gold foil and an uncoated optical fiber end face. The sensing structure shows high sensitivity to wide-bandwidth acoustic waves, and thus we were able to demonstrate SPM imaging in air. Moreover, by setting different focal lengths (FLs) of AFLs, we were able to distinguish signals from multiple sensors, thereby realizing multiplexing of sensors. Finally, we obtained 2D images of seismic physical models (SPMs) by reconstructing the recycled ultrasonic signals using a time-of-flight approach.

2. Sensor Fabrication and Sensing Mechanism

Fig. 1(a) demonstrates the structure and ultrasonic detection mechanism of the sensor. The sensor was formed by the following detail processing. A standard single mode fiber (SMF) with a flat cleaved end-face was inserted into the center hole of a ceramic tube terminated by a 130 nm-thick gold foil. An AFL was placed at the end of the surrounding plastic ferrule to focus the acoustic field onto the gold film. The plano-concave AFL was machined from PMMA, which was suitable owing to its small acoustic impedance of 3.1 kg/(m^3·s). Besides, focusing acoustic waves by spherical lenses is realized, in which a plano-concave lens will focus a plane wave. Photographs of three 6 mm-diameter sample AFLs are shown in Fig. 1(c). The FLs of the three lenses were 9 mm, 16 mm and 23 mm. A length of SMF leading to and from the ceramic ferrule was protected by a thin steel tube. Thin gold foil was selected as the FPI mirror for two reasons: the highly reflectivity, which improves the reflectivity of the sensor, and the 130 nm thickness of the foil, which makes it sensitive to the weak acoustic pressure. During the sensor fabrication, the end-face of ceramic tube was kept contaminant-free to make the foil to be adhered tightly due to the van der Waals force. In this structure, the fragile fiber and gold foil were well-protected by both the ceramic ferrule and a lens, ensuring that the sensing probe is rugged and stable during scanning of SPMs. Fig. 1(d)–(g) demonstrate the fabrication process and sensing mechanism of the sensor. As the device was produced, the surfaces of the SMF and gold film formed a FPI with a cavity length of 100 μm. The AFL improves the coupling efficiency of acoustic wave to sensor by focusing the acoustic pressure onto the gold foil. The photograph of the integrated sensor structure is shown in Fig. 1(b).
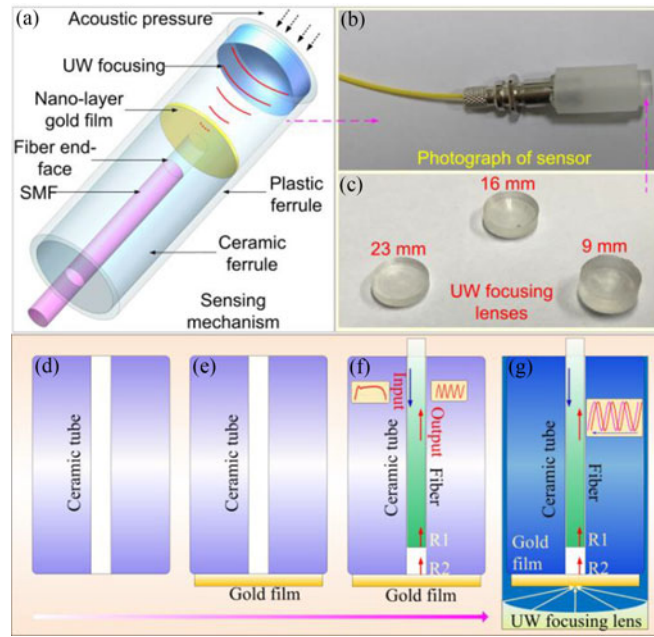
Fig. 1. Sensor fabrication. (a) Schematic diagram of the UW sensor structure. (b) Photograph of the fabricated sensor. (c) Photograph of several UW focusing lenses made of polymethyl methacrylate (PMMA). (d)–(g) sensor fabrication process and UW sensing mechanism.

Fig. 2. (a) Schematic diagram of acoustic focusing and theoretical simulations on (b) acoustic pressure level (APL) of AFL, in which red is high, grey is low, and blue is lowest level. (c) Normalized APL along the radius of acoustic focusing lens at the position of gold foil.

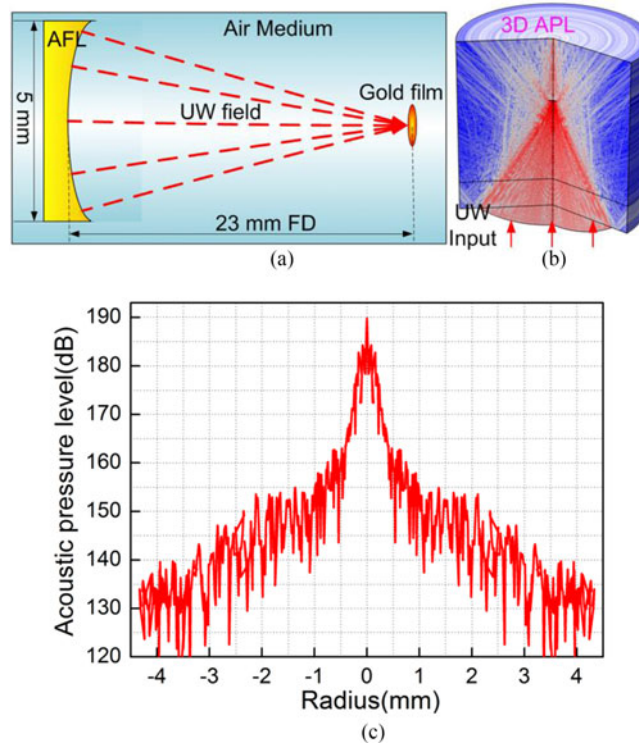In Fig. 2, the acoustic focusing performance of the AFL was simulated by using the software of COMSOL Multiphysics. The simulations were finished by solving the homogeneous Helmholtz (1) [26] in axisymmetric cylindrical coordinates:

$$\frac{\partial}{\partial r}\left[-\frac{r}{\rho_c}\left(\frac{\partial p}{\partial r}\right)\right] + r\frac{\partial}{\partial z}\left[-\frac{\partial}{\partial \rho_c}\left(\frac{\partial p}{\partial z}\right)\right] - \left[\left(\frac{\omega}{c_c}\right)^2\right]\frac{rp}{\rho_c} = 0 \tag{1}$$

where r and z are the radial and axial coordinates, p is the acoustic pressure, and ω is the angular frequency. The density, ρ_c, and the speed of acoustic wave, c_c, are complex-valued to account for the damping properties of the materials. In (1), we assume that the acoustic wave propagation is linear and also the amplitude of shear waves in the air is much smaller than that of the pressure waves. Nonlinear effects and shear waves are therefore neglected.

In the simulation, the acoustic source was assumed to be a 300 kHz plane wave propagating at 340 m/s in air with a referenced acoustic pressure of 20 μPa. The FL of the AFL was 23 mm with the gold foil at the focal point, as shown in Fig. 2(a). Fig. 2(b) shows the acoustic pressure level (APL) in 3D dimensional cylindrical coordinates of the model. It is clearly seen that the main acoustic pressure is focusing on the specified position (gold foil), although the weak acoustic scattering appears as well in the propagation route. Our model shows that the APL at the focal point is much larger than that of the other positions, resulting in an approximately improvement of 60 dB [shown in Fig. 2(c)]. Besides, as mentioned in reference [27], [28], the focal spot size of the acoustic lens is calculated as 1.7 mm. In the proposed sensor, the focal spot size of the acoustic lens is key parameter. The smaller focal size may improve further acoustic focusing effect and then promote the sensitivity of sensor. Here the material of PMMA is taken as a case for acoustic production. It is also possible to select more suitable materials to further improve the performance of acoustic lens in the future work. Moreover, this effect not only promotes the coupling of the acoustic wave onto the gold foil, but also plays an important function in adjusting time delay of the response of the sensor to the acoustic wave. Because the acoustic wave propagates more slowly in air than in liquid and solid, a small change in the air gap length between the lens and the foil can make a measurable difference in the time delay of the received acoustic signal. By selecting different FLs and air gap lengths, we were able to time-division multiplex several sensors as described in Section 3.

We have theoretically modeled the ultrasonic response of the sensor by analyzing the interaction between acoustic pressure and the optical interference. To simplify the discussion, we only consider the axial strain induced by acoustic wave and ignore shear stress since the sensor structure is the cylindrically symmetric and the gold foil is very flexible and its thickness is less that 1/1000th of the acoustic wavelength. As the acoustic wave propagates through the air as a longitudinal compressional wave it periodically deforms the gold foil. Since the wavelength of the acoustic wave (typically 0.1 mm to 1.0 mm) is much larger than the sensing region of the gold foil, the acoustic wave can be regarded as a plane wave. When the acoustic wave reaches to the sensor, the most of the power is reflected at the air-to-film interface owing to the large acoustic impedance difference of the gold foil and air, 18.9×10^6 kg/(m^2·s) for gold foil and 0.0004×10^6 kg/(m^2·s) for air. The interaction force makes the foil deformation, resulting in the cavity length variation of the sensor. Acoustic wave frequency is determined by the acoustic source of PZT, and thus the time-varying output intensity of sensor is determined by the amplitude of the acoustic pressure. In addition, it is because the low reflectivity of fiber end-face, the FPI can be simplified as a dual-wave interference (the forward-propagated light is reflected by the two surfaces of fiber end-face and gold film surface), and finally produce a well-defined interference spectrum.

Moreover, the performances of sensor were characterized in the simulations according to the equation derivations [29]. The interference mechanism could be simplified as the dual-beam interference of between fiber end-face reflection and gold film reflection. A sinusoidal interference spectrum was achieved as shown in Fig. 3(a), which presents a large linear spectral slope. Fig. 3(b) demonstrates FPI cavity length versus the acoustic pressure statically. It can be seen that the selected spectral feature moved approximately 1.8 nm with the acoustic pressure increasing from 0 psi to 0.03 psi. In Fig. 3(c), the cavity length of the sensor was plotted as a function of acoustic
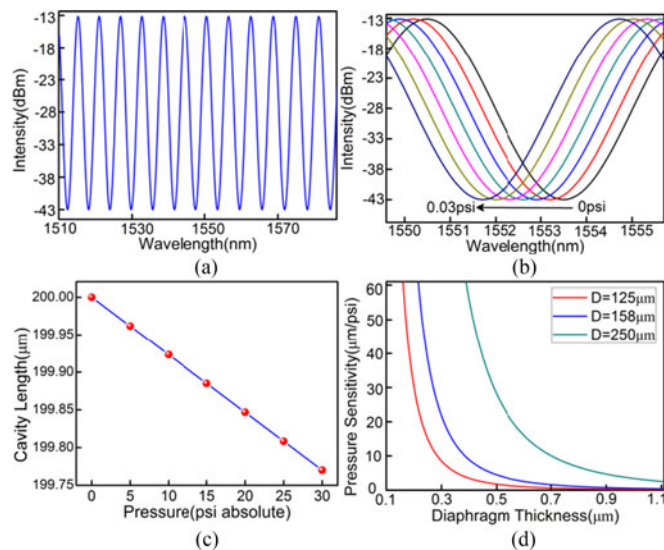
Fig. 3. Theoretical calculations on (a) interference spectrum pattern, (b) one interference dip blue-shift versus acoustic pressure at 300 kHz, (c) cavity lengths of sensor versus acoustic pressure, and (d) pressure sensitivity as function of thickness of gold foil under the different cavity lengths.

pressure. The original, unperturbed cavity length of 200 μm decreased to 199.77 μm as the acoustic pressure increased from 0 psi to 30 psi. When the acoustic wave is exerted on the sensor, i.e., dynamically pushing the gold foil, the length of FPI cavity will change in the frequency of acoustic wave. As the result, the amplitude-frequency information of acoustic wave can be achieved by reflection light intensity interrogation using spectral side-band filtering technology. The thickness of gold foil is another key factor that influences the sensitivity of sensor. Fig. 3(d) demonstrates the simulation result of acoustic pressure sensitivity as the function of gold foil thickness. As the gold foil thickness decreases, the sensitivities of three sensors, each with a different unperturbed FP cavity length, all increase slowly first and then sharply increase. For the different cavity lengths, the high sensitivity regions differ: for 250 μm cavity length, the foil thickness should be smaller than 0.7 μm, for 158 μm, the foil thickness smaller than 0.4 μm, and for 125 μm, the foil thickness smaller than 0.3 μm. The result in Fig. 3(d) can be understood by the equation in [20], in which ultrasonic sensitivity, S, is directly proportional to $1/h^3$ (h is thickness of gold foil). These simulation results in Fig. 3 provide the good references for setting the structure parameters of sensor. In practical applications, we should make a trade-off between the frequency range and sensitivity of the sensor by choosing the suitable structure parameters of the sensor length and the thickness and diameters of the gold foil.

3. Experimental Results and Discussion

The schematic configuration of the ultrasonic imaging system is shown in Fig. 4(a). A tunable laser (Santec-710) with a 100 kHz linewidth and a 0.1 pm tunable resolution was employed as the light source, and light was launched into the sensing probe through a coupler. The reflection of the sensor was monitored by a photodiode (PD, New Focus, California, US) with a bandwidth of 10 MHz at a 0 dBm gain, and finally the detection signal was collected by a data acquisition card for analysis. Before implementing the scanning detection of the acoustic wave reflected by the SPM, the responses of the sensor to acoustic wave and multiplexing of sensor in air were characterized. Once the fiber FPI was achieved, a well-defined interference spectrum was obtained, as shown in Fig. 4(d). Using the spectral side-band filtering technique in Fig. 4(a), we were able to get the ultrasonic responses of sensors. In this process, the sensor was held on a moving stage, and the PZT source, providing ultrasonic pulses at frequency of 300 kHz and repetition frequency of 1 kHz.
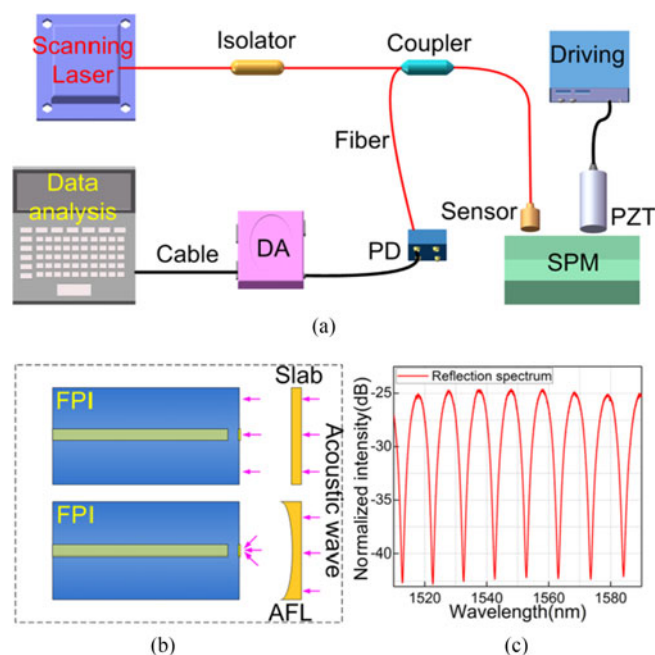
Fig. 4. Schematic configuration of experiment setup for UW imaging. SPM is the physical model, PD is the optical power detector, and DA is the data acquisition card.

The centers of the sensor and PZT were kept in the same line. The distance between the sensor and PZT were precisely controlled by the moving stage. The detailed schematic diagrams of experiment operations are shown in Fig. 4(b) and (c). Compared with the previous works, here the highlight of this work is utilizing designed AFL to further promote the coupling efficiency of acoustic-to-sensor as well as realize the time-domain multiplexing.

In the experiments, in comparison, we fabricated the different sensors with the AFLs and PMMA slab, in which FLs of AFLs and air gaps between FPI and slab were 9 mm, 16 mm and 23 mm and with the same thickness, respectively. Fig. 5(a) demonstrate the time domain spectra changes of the sensors with slab and AFLs at a fixed acoustic frequency of 300 kHz (which is one of ultrasonic frequency commonly used in SPM imaging of centimeter-order precision). We saw the peak-to-peak voltages of detection signal of sensors with AFLs were 3.26 V for 9 mm FL, 3.24 V for 16 mm FL, and 3.24 V for 23 mm FL. In contrast, the detection signals of the sensors with PMMA slab (without acoustic focusing effect) had smaller the peak-to-peak voltages, 1.81 V for 9 mm air gap, 1.39 V for 16 mm air gap, and 1.19 V for 23 mm air gap. The peak-to-peak voltages of detection signals versus the FLs and air gaps are plotted here, as shown in Fig. 5(b). We clearly saw that signal intensities of slab-based sensor sharply decrease down to the small value with air gap increasing. In comparison, the signal intensities of the AFL-based sensor present slightly decrease with the FL increasing. The results well identify the AFL component effectively increases the acoustic wave sensitivity of sensor and ensures the stability of sensor. Besides, given the noise voltage of 2 mV and signal peak-to-peak voltage of 3.26 V [achieved in the red curve of Fig. 5(a)], the signal-to-noise ratio of the sensor with AFL is calculated as 96.37 dB, which is larger than that of previous works (27.96 dB for FBG-FP [30] and 24.08 dB for Micro-bubble FPI [31]).

Because of the slow transmission speed of acoustic wave in air, the small difference between two acoustic signals in air could make a large time delay, which made us distinguish signal sources in the time domain. Utilizing the time delay effect, it was possible to multiplex several fiber FPIs for acoustic wave detection, i.e., realizing the time division multiplexing. In Fig. 5(a), it was seen that the detection signals presented the obvious time differences, which allowed us to easily distinguish
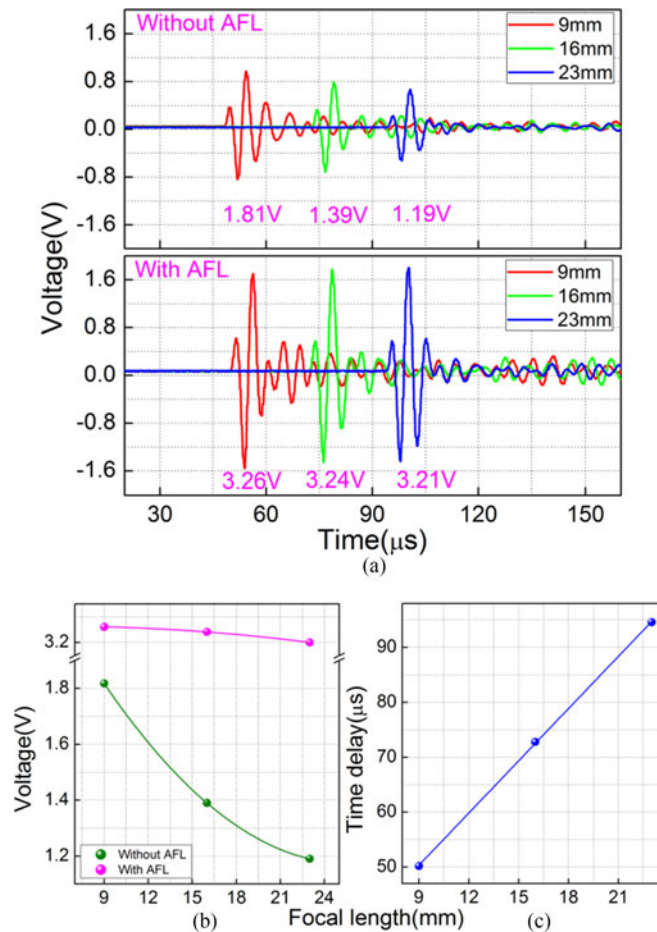
Fig. 5. Responses to (a) 300 kHz pulse acoustic waves of sensor without AFL and with AFLs of 9 mm, 16 mm, and 23 mm. (b) Time delays to 300 kHz pulse acoustic as functions of FLs of the AFLs. (c) Signal intensity versus air gaps with AFL and without AFL application.

the sensors. Different from the other reported acoustic wave sensor multiplexing technologies [32]–[35], which usually used the ultra-long fiber to delay the arrival time of light signal, the method in this manuscript used different FLs of AFLs to delay the arrival time of the acoustic waves. The success key was the ultra-high acoustic sensitivity of the FPI, which made the sensor suitable acoustic wave detection in air. Here the time delays of the three sensors were plotted as function of AFL's FLs, as shown in Fig. 5(c). With the FL increasing from 9 mm to 23 mm, the time delays also increase from 50.2 μs to 94.6 μs, which are totally determined by the acoustic wave propagation distances in air. This time delay effect to acoustic wave propagation makes it possible to multiplex the fiber device as the sensing arrays, as well with the support by the AFLs making sure the sensitivities of sensors.

Moreover, in order to characterize the frequency of acoustic wave signal, the time domain spectrum detected by the AFL-based sensor [i.e., red curve shown in Fig. 4(a)] was transferred to the frequency spectrum using Fourier transform technology, as shown in Fig. 6. It was seen that the main frequency of acoustic signal is 300 kHz, which was well agreed with the main frequency of acoustic wave of PZT emission. The low frequency noises appearing in the frequency spectrum are owing to the sensor responds to the unwanted frequency band of PZT emission. The phenomenon also presented the sensor had a wide frequency band response to acoustic wave. The unwanted low frequency noises would be filtered out in digital domain, when the scanning images were reconstructed in the following section.
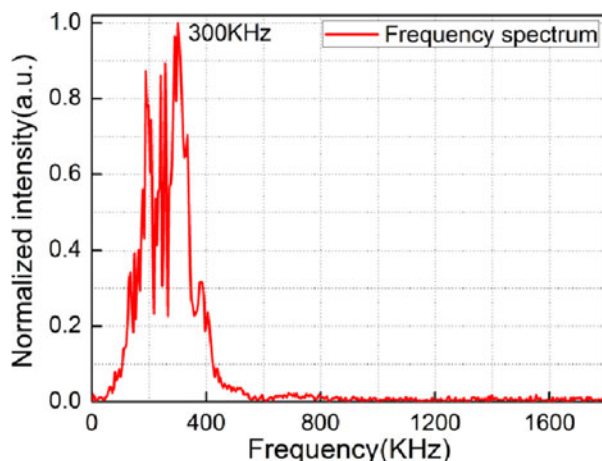
Fig. 6. Frequency spectrum of acoustic signal that is Fourier transformed time spectrum.
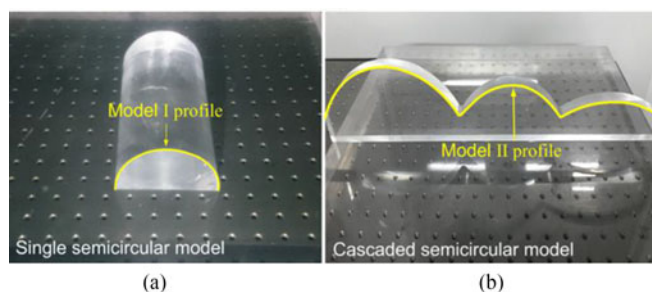

Fig. 7. Photographs of two physical models. (a) Single semicircular model. (b) Cascaded semicircular model.

After the performance study of the sensor probe, we demonstrated SPM imaging as follows. The experimental diagram of ultrasonic imaging on SPM is shown in Fig. 4(a). The sensor and PZT were held on a moving stage together and kept a fixed distance of 3 cm apart. The downward-facing sensor and PZT were scanned in a plane parallel to the table supporting the SPM. The PZT launched the pulsed acoustic wave to the SPM, and the sensor detected the reflected acoustic intensity as a function of time. The whole scanning process was performed in air. We tested models of two different shapes PMMA models, as shown in Fig. 7. Model I was a single 10 cm radius solid half-cylinder. Model II was a cascaded set of three circular segments of radius of 2 cm, 4 cm and 6 cm. The PZT source and sensor were moved quasi-continuously with a step of 0.1 mm for point-to-point scanning. The air gap between the sensor and the highest position of model was 5 cm. The acoustic wave was mainly reflected by the interface between air and models, i.e., the upper surfaces of the models. The small transmitted portion of the acoustic waves propagated through the models and reflects from discontinuities within the model. From the known acoustic transmission velocity in air (340 m/s) and PMMA (2700 m/s), the thickness and discontinuities positions could be determined. By scanning the models and reconstructing the 2D images, we determined the shape, size and inner structures of the models.

Fig. 8 present the ultrasonic images of the above SPMs, which were reconstructed by the time-of-flight approach. As expected, the images clearly show that, for the first model, the two surfaces of the semicircular cross-section model were clearly achieved, and for second model, the surface outlines of the cascaded model and their difference were also performed, which were in good agreement with the real model structures in Fig. 7. Besides, it is because the acoustic impedance difference of air and PMMA model, 0.0004×10^6 kg/(m^2·s) for air and 1.48×10^6 kg/(m^2·s) for model [36], the reflection coefficient would give up to 99.94% in certain transmission depth. The
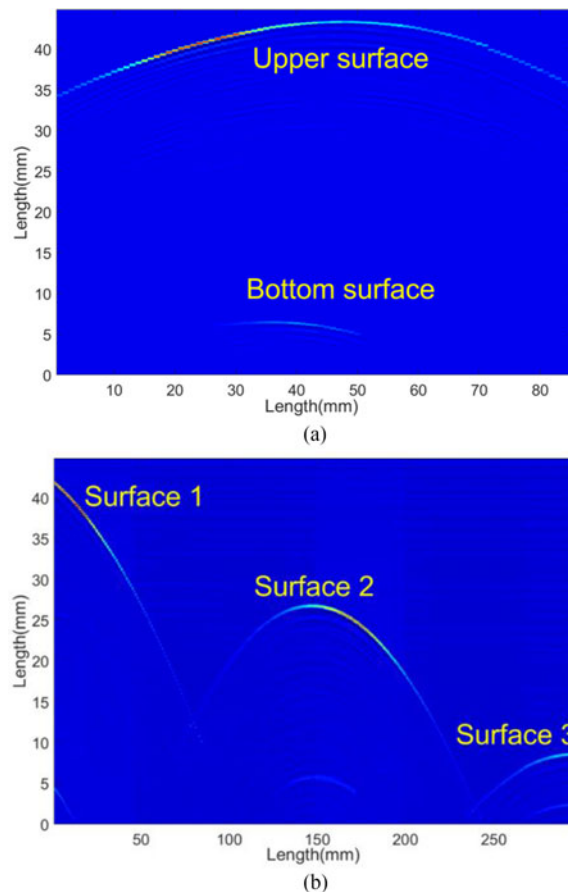
Fig. 8. Images of physical models. (a) Single half-cylinder model. (b) Cascaded semicircular model.

acoustic signal reflected by the upper surface of model is therefore much stronger than that by the bottom surface.

In our prior work [30], the ultrasonic images of SPMs were realized using a fiber Bragg grating (FBG)-FP-based sensor. However, although acoustic focusing technology was employed to improve the performance of the sensor, the sensitivity was not high enough and the whole ultrasonic scanning process could not be implemented in air owing to the large acoustic attenuation loss of air. In general, the acoustic attenuation coefficient of air at 300 kHz are 0.108 dB/cm, respectively, which are three orders of magnitude larger than those of water (1.8×10^{-4} dB/cm at 300 kHz) [37]. The keys to success of the proposed sensor here are the ultra-high sensitivity to the weak acoustic field and artful structure for the coupling of acoustic-to-fiber. Especially, the AFL focuses the acoustic wave on the gold foil, which not only improves the sensitivity of sensor, but also flexibly adjusts arrival time of acoustic wave by changing the FL of AFL. The excellent performance of this sensor makes it a good candidate for non-contact imaging of SPMs in air.

Besides, as expected, the surfaces and boundaries of the two physical models are imaged clearly by reconstructing their reflecting acoustic signal. In our experiment, the models were placed in air which largely simplifies the imaging system. The high-precision imaging of the SPM is determined by two factors. One is the sensor structure itself. During the scanning process, the compact size (with an effective sensing diameter of 125 μm) and the good directivity of the sensing structure give the sensor a high spatial resolution, which will be important for the imaging of the small defects in real rock models. The other factor is the noise removal. It is necessary to employ a band-pass filter near 300 kHz for removing the unwanted noise frequencies coming from the surrounding electromagnetic interference and the PZT resonance. In addition, we can find that the amplitude

distributions of the two reconstructed images are inhomogeous, i.e., the middle part is larger than that of two sides of models. There are several reasons for this result: the different air gaps between sensor and scanning positions on the models (which induce different acoustic attenuation loss), the different detection directions that the circular arc surfaces of models partly reflect the acoustic waves to sensor, the oblique incidence-induced wave conversion loss (especially at the both sides of models, the large oblique incidence could produce shear wave in the model that will fully loss out), and parts of the acoustic wave scattered away by the sharp corner (with the size that is comparable to or smaller than the 1.13 mm wavelength of acoustic wave), decreasing the intensity of reflection wave. In addition, there are small surfaces appear between two main surfaces in Fig. 8. We can consider this phenomenon as a form of reverberation. In the presence of two reflective interfaces, the echoes generated from the main beam may be repeatedly reflected, in repeated trips before go back to the sensor, where they may be detected. Each echo is received erroneously transcribed as a band located at a greater depth, so we may see multiple parallel lines of decreasing intensity and equidistant from each other. Anyway, the clear profiles of the two models are achieved by our proposed sensor.

4. Conclusion

In this paper, we developed a multiplexed interferometer using the acoustic lens that could effectively focus the acoustic wave to the sensing surface (improving the ultrasonic wave sensitivity), and realized non-contact ultrasonic imaging of seismic-physical-models in air. The interrogation of the sensor only requires one power detector together with a tunable laser and side-band filter. 2D images of two polymethyl methacrylate model blocks were reconstructed by the proposed ultrasonic scanning system. Compared with the piezoelectric transducers imaging device and hydrophone, the fiber FPI probe provides excellent performances using a smaller structure, high sensitivity and good multiplexing capability.

References

[1] M. R. E. Lamont, Y. Okawachi, and A. L. Gaeta, "Route to stabilized ultrabroadband microresonator-based frequency combs," *Opt. Lett.*, vol. 38, no. 18, pp. 3478–3481, 2013.

[2] A. Bakulin, V. Grechka, and I. Tsvankin, "Estimation of fracture parameters from reflection seismic data—Part I: HTI model due to a single fracture set," *Geophys.*, vol. 65, no. 6, pp. 1788–1802, 2000.

[3] M. Urosevic, G. Bhat, and M. H. Grochau, "Targeting nickel sulfide deposits from 3D seismicreflection data at Kambalda Australia," *Geophys.*, vol. 77, no. 5, pp. WC123–WC132, 2012.

[4] C. H. Jones, H. Reeg, G. Zandt, H. Gilbert, T. J. Owens, and J. Stachnik, "P-wave tomography of potential convective downwellings and their source regions Sierra Nevada California," *Geosphere*, vol. 10, no. 3, pp. 505–533, 2014.

[5] S. Dou, S. Nakagawa, D. Dreger, and J. Ajo-Franklin, "A rock-physics investigation of unconsolidated saline permafrost: P-wave properties from laboratory ultrasonic measurements," *Geophys.*, vol. 81, no. 1, pp. WA233–WA245, 2016.

[6] S. Park and S. He, "Standing wave brass-PZT square tubular ultrasonic motor," *Ultrasonics*, vol. 52, no. 7, pp. 880–889, 2012.

[7] K. Yamashita, T. Nishiumi, K. Arai, H. Tanaka, and M. Noda, "Intrinsic stress control of sol-gel derived PZT films for buckled diaphragm structures of highly sensitive ultrasonic microsensors," *Procedia Eng.*, vol. 120, pp. 1205–1208, 2015.

[8] D. Y. Bae and J. R. Lee, "A health management technology for multisite cracks in an in-service aircraft fuselage based on multi-time-frame laser ultrasonic energy mapping and serially connected PZTs," *Aerosp. Sci. Technol.*, vol. 54, pp. 114–121, 2016.

[9] A. D. Kersey *et al.*, "Fiber grating sensors," *J. Lightw. Technol.*, vol. 15, no. 8, pp. 1442–1463, Aug. 1997.

[10] B. Culshaw, G. Thursby, D. Betz, and B. Sorazu, "The detection of ultrasound using fiber-optic sensors," *IEEE Sens. J.*, vol. 8, no. 7, pp. 1360–1367, Jul. 2008.

[11] Y. Okabe and Q. Wu, "Using optical fibers for ultrasonic damage detection in aerospace structures," in *Structural Health Monitoring in Aerospace Structures*. Amsterdam, The Netherlands: Elsevier, 2016, pp. 95–118.

[12] L. Y. Shao *et al.*, "High-frequency ultrasonic hydrophone based on a cladding-etched DBR fiber laser," *IEEE Photon. Technol. Lett.*, vol. 20, no. 8, pp. 548–550, Apr. 2008.

[13] Z. X. Li, L. Pei, B. Dong, C. Ma, and A. B. Wang, "Analysis of ultrasonic frequency response of surface attached fiber Bragg grating," *Appl. Opt.*, vol. 51, no. 20, pp. 4709–4714, 2012.

[14] J. R. Lee and H. Tsuda, "Fiber optic liquid leak detection technique with an ultrasonic actuator and a fiber Bragg grating," *Opt. Lett.*, vol. 30, no. 24, pp. 3293–3295, 2005.

[15] G. Wild and S. Hinckley, "Acousto-ultrasonic optical fiber sensors: Overview and state-of-the-art," *IEEE Sens. J.*, vol. 8, no. 7, pp. 1184–1193, Jul. 2008.

[16] J. F. Dorighi, S. Krishnaswamy, and J. D. Achenbach, "Stabilization of an embedded fiber optic Fabry-Perot sensor for ultrasound detection," *IEEE Trans. Ultrason. Ferroelectr. Freq. Control*, vol. 42, no. 5, pp. 820–824, Sep. 1995.

[17] C. Koch, "Measurement of ultrasonic pressure by heterodyne interferometry with a fiber-tip sensor," *Appl. Opt.*, vol. 38, no. 13, pp. 2812–2819, 1999.

[18] F. Guo, T. Fink, M. Han, L. Koester, J. Turner, and J. S. Huang, "High-sensitivity, high-frequency extrinsic Fabry-Perot interferometric fiber-tip sensor based on a thin silver diaphragm," *Opt. Lett.*, vol. 37, no. 9, pp. 1505–1507, 2012.

[19] F. Xu, J. H. Shi, K. Gong, H. F Li, R. Q. Hui, and B. L. Yu, Fiber-optic acoustic pressure sensor based on large-area nanolayer silver diaghragm," *Opt. Lett.*, vol. 39, no. 10, pp. 2838–2840, 2014.

[20] J. Xu, X Wang, K. L. Cooper, and A. Wang, "Miniature all-silica fiber optic pressure and acoustic sensors," *Opt. Lett.*, vol. 30, no. 24, pp. 3269–3271, 2005.

[21] P. Morris, A. Hurrell, A. Shaw, E. Zhang, and P. Beard, "A Fabry-Perot fiber-optic ultrasonic hydrophone for the simultaneous measurement of temperature and acoustic pressure," *J. Acoust. Soc. Amer.*, vol. 125, no. 6, pp. 3611–3622, 2009.

[22] M. Massot-Campos and G. Oliver-Codina, "Optical sensors and methods for underwater 3D reconstruction," *Sensors*, vol. 15, no. 12, pp. 31525–31557, 2015.

[23] F. Blais, "Review of 20 years of range sensor development," *J. Electron. Imag.*, vol. 13, no. 1, pp. 231–243, 2004.

[24] M. S. Miller, R. W. Phillips, S. D. Hahn, and J. H. Scholz, "Time rate of decay optical fiber total air temperature sensor and optically interfaced air data system for fly-by-light applications," in *Proc. SPIE's Symp. OE/Aerosp. Sens. Dual Use Photon.*, 1995, pp. 182–186.

[25] L. Richards, A. R. Parker, W. L. Ko, and A. Piazza, "Real-time in-flight strain and deflection monitoring with fiber optic sensors," presented at the Space Sens. Meas. Techn. Workshop, Nashville, TN, USA, 2008.

[26] M. Nadjafikhah and A. Mahdipour-Shirayeh, "Symmetry analysis of cylindrical Helmholtz equation," *Insect Biochem.*, vol. 10, no. 3, pp. 289–303, 2009.

[27] Q. Z. Rong *et al.*, "UW imaging of seismic-physical-models in air using fiber-optic Fabry-Perot interferometer," *Sensors*, vol. 17, no. 2, 2017, Art. no. 397.

[28] G. Maes, M. Delaide, and P. Dombret, "On the use of the ultrasonic beam focusing technique," in *Proc. 11th Int. Conf. NDE Nucl. Pressure Vessel Ind.*, Albuquerque, NM, USA, 1992, R&D no: 47-3–0027-4.

[29] H. Azhari, *Basics of Biomedical Ultrasound for Engineers*. Hoboken, NJ, USA: Wiley, 2010, pp. 144–146.

[30] T. Gang *et al.*, "High-frequency fiber-optic ultrasonic sensor using air micro-bubble for imaging of seismic physical models," *Sensors*, vol. 16, no. 12, 2016, Art. no. 2125.

[31] Q. Z. Rong *et al.*, "Ultrasonic imaging of seismic physical models using fiber bragg grating fabry–perot probe," *IEEE J. Sel. Topics Quantum Electron.*, vol. 23, no. 2, Mar./Apr. 2017, Art. no. 5600506.

[32] F. Dones and D. Varshneya, "Overview of time division multiplexing sensor technology," in *Proc. SPIE's Int. Symp. Opt., Imag., Instrum.*, 1994, pp. 84–93.

[33] L. Deitrich, "Method and apparatus for controlling transducer multiplexing in ultrasound imaging system," *Acoust. Soc. Amer. J.*, vol. 100, 1996, Art. no. 3490.

[34] M. Carpenter, W. Rashid, M. Ghovanloo, D. Cowell, S. Freear, and L. Degertekin, "Time-division multiplexing for cable reduction in ultrasound imaging catheters," in *Proc. IEEE Biomed. Circuits Syst. Conf.*, 2015, pp. 1–4.

[35] C. Peng, X. Gao, Li Wang, Y. Zhang, J. Peng, and K. Yang, "Ultrasonic signal multiplex technology for dynamic wheelset defect detection system," in *Proc. Int. Conf. Inf. Technol., Comput. Eng. Manage. Sci.*, vol. 1, 2011, pp. 260–262.

[36] M. Rowlands, "Acoustic properties of PMMA: Towards Bragg gratings in ultrasonic particle separation," Final Year Project thesis, School Mech. Chem. Eng., Univ. Western Australia, Crawley, W.A., Australia, 2011.

[37] P. N. T. Wells, "Ultrasonic imaging of the human body," *Rep. Prog. Phys.*, vol. 62, no. 5, pp. 671–722, 1999.